RESEARCH ARTICLE

JBMR®

Dual-Layer Spectral–Computed Tomography Enhances the Separability of Calcium-Based Implant Material from Bone: An Ex Vivo Quantitative Imaging Study

Jaime A. Peña,[1] Jonathan L. Shaul,[2] Michael Müller,[3] Timo Damm,[1] Reinhard Barkmann,[1] Bodo Kurz,[4] Graeme M. Campbell,[5] Sandra Freitag-Wolf,[6] and Claus-C. Glüer[1]

[1]Section Biomedical Imaging, Department of Radiology and Neuroradiology, University Medical Center Schleswig-Holstein (UKSH), Kiel, Germany
[2]Agnovos Healthcare, Rockville, MD, USA
[3]Clinic for Orthopedics and Trauma Surgery, University Medical Center Schleswig-Holstein (UKSH), Kiel, Germany
[4]Department of Anatomy, Christian-Albrechts University (CAU), Kiel, Germany
[5]Philips GmbH Market DACH, Hamburg, Germany
[6]Institute of Medical Informatics and Statistics, Christian-Albrechts University (CAU), Kiel, Germany

ABSTRACT

Local treatment of bone loss with an injection of a resorbable, calcium-based implant material to replace bone has a long history of clinical use. The in vivo discrimination of changes in bone versus implant is challenging with standard computed tomography (CT). However, spectral-CT techniques enable the separation between tissues of similar densities but different chemical compositions. Dual-layer spectral-CT imaging and postprocessing analysis methods were applied to investigate the separability of AGN1 (a triphasic calcium-based implant) and bone after AGN1 injection in $n = 10$ male cadaveric femurs ex vivo. Using the area under the curve (AUC) from receiver-operating characteristic (ROC) analyses, the separability of AGN1 from bone was assessed for AGN1 (postoperatively) versus compact and versus femoral neck cancellous bone (both preoperatively). CT techniques included conventional Hounsfield (HU) and density-equivalent units (BMD, mg hydroxyapatite [HA]/cm^3) and spectral-CT measures of effective atomic number (Zeff) and electron density (ED). The samples had a wide range of femoral neck BMD (55.66 to 241.71 mg HA/cm^3). At the injection site average BMD, HU, Zeff, and ED increased from 69.5 mg HA/cm^3, 109 HU, 104.38 EDW, and 8.30 Zeff in the preoperative to 1233 mg HA/cm^3, 1741 HU, 181.27 EDW, and 13.55 Zeff in the postoperative CT scan, respectively. For compact bone at the femoral shaft the preoperative values were 1124.15 mg HA/cm^3, 1648 HU, 177 EDW, and 13.06 Zeff and were maintained postoperatively. Zeff showed substantially sharper distributions and significantly greater separability compared to ED, BMD, and HU (all $p < 0.002$, for both regions) with average AUCs for BMD, HU, ED, and Zeff of 0.670, 0.640, 0.645, and 0.753 for AGN1 versus compact and 0.996, 0.995, 0.994, and 0.998 for AGN1 versus femoral neck cancellous sites, respectively. Spectral-CT permits better discrimination of calcium-based implants like AGN1 from bone ex vivo. Our results warrant application of spectral-CT in patients undergoing procedures with similar implants. © 2022 The Authors. *Journal of Bone and Mineral Research* published by Wiley Periodicals LLC on behalf of American Society for Bone and Mineral Research (ASBMR).

KEY WORDS: CALCIUM-BASED RESORBABLE IMPLANTS; FEMUR AUGMENTATION; SPECTRAL-CT; ZEFF; EFFECTIVE ATOMIC NUMBER; OSTEOPOROSIS

Introduction

Background of the study

Resorbable materials can be used to induce new bone formation to strengthen skeletal sites like the proximal femur.[1] Implant materials with mechanical properties closer to native bone may be preferred to rigid augmentation procedures; e.g., with nails or screws such as to minimize stress-concentrations. A mismatch between mechanical properties of bone and metallic implants may not yield the expected protection benefit and may even decrease bone strength (of a treated femur).[2]

Calcium-based implant materials comprise a wide range of compositions (from single to multiphase components) with varying resorption rates from quickly resorbable to long-lasting.

Received in original form April 13, 2022; revised form August 22, 2022; accepted September 17, 2022.
Address correspondence to: Jaime A. Peña, MSc., Section Biomedical Imaging, Department of Radiology and Neuroradiology, University Medical Center Schleswig-Holstein (UKSH), Am Botanischen Garten 14, D-24118, Kiel, Kiel, Germany. E-mail: jaime.pena@rad.uni-kiel.de
Additional Supporting Information may be found in the online version of this article.
Journal of Bone and Mineral Research, Vol. 37, No. 12, December 2022, pp 2472–2482.
DOI: 10.1002/jbmr.4710

Calcium-based synthetic bone substitutes have a long history of clinical use and have been reported to facilitate bone formation.[3] Advantages of calcium-based materials are the simplicity of application during surgeries and their resorption and stimulation of bone formation under physiological conditions.[4] In particular, materials based on calcium phosphate have been widely studied as bone substitutes owing to the similarity to bone composition.[5] Recently, a triphasic calcium-based implant material (AGN1) has been used to treat bone loss in the proximal femurs of women with osteoporosis resulting in bone mineral density increases observed out to a final time point of 5 to 7 years.[1] Injection of AGN1 improved mechanical properties in cadaveric femurs[6] and vertebrae.[7] In preclinical models, both microCT and histopathology demonstrated resorption and replacement of the implant material with bone.[8,9] However, similar resorption and replacement shown during clinical evaluation[1] relied solely on imaging techniques and has not been confirmed using histopathology. In the absence of histopathology, the separation of resorbable implant materials and bone remains challenging with standard imaging techniques.

There is a lack of tools to monitor such implant behavior in vivo. New clinical and preclinical magnetic resonance imaging (MRI) sequences like ultrashort and zero echo time (UTE and ZTE, respectively) have been developed for hard tissues like bone.[10,11] However, MRI-scans do not yield a mineral density measurement directly and studies performed have not yet demonstrated image quality sufficient to judge the implant material status. Current quantitative computed tomography (QCT) techniques can yield estimates of bone mineral density (BMD). However, because of the close resemblance in the X-ray absorption properties of the implant components like calcium phosphates and calcium sulfates and those of bone (mineral constituents based mainly on hydroxyapatite [HA]) the separation between implant and bone and subsequent quantification using QCT is challenging.

Dual-energy and spectral-CT methods

In the last two decades, dual-energy CT (DECT) techniques have emerged in the clinical setting as a tool to enhance the separation between tissues with similar densities or values in Hounsfield units (HU), provided that they show sufficiently different spectral X-ray absorption characteristics. There are different configurations for DECT devices depending on the CT manufacturer. Such configurations include dual-source, single-source with rapid kilovolt (kV) switching, single-source with split-filter or a single-source with a dual-layer detector. The latter configuration, is the closest to a photon-counting CT-system because the low and high energy photons from a single polychromatic X-ray beam can be separated simultaneously in one CT scan.[12] It has been thus referred to as dual-layer spectral-CT (DLSCT). A DECT application based on a dual-layer spectral-CT device (termed hereafter spectral-CT) was used for the present study.

By using X-ray spectra obtained at two different and sufficiently separated energies, spectral-CT permits materials separation through algorithms that model the X-ray photons' interaction processes with matter. Outcomes of such decomposition algorithms include effective atomic number (Zeff) and electron density (ED) maps.[13] Zeff and ED derivations can be performed in projection space or in image space.[13-17] The actual algorithm used in a CT device is proprietary but Zeff and ED measurements from projection space have been reported to be more accurate than in image space.[18]

Earlier DECT-based implementations of Zeff focused on values between 5 and 15.[14] More recently, manufacturers can provide Zeff maps with voxel values from 5 up to 30. This is a range that mostly represents human tissues and includes elements relevant for bone and the implant materials covered in this contribution: phosphorus at $Z = 15$, sulfur at $Z = 16$, and calcium at $Z = 20$. According to the spectral-CT manufacturer used in this study, air has a Zeff value of 0; fat, water, and cortical bone have Zeff of 5.9, 7.4, and 13.2, respectively.[19] The accuracy of Zeff values was measured to be within 0.2 Zeff units by using calibration phantoms containing iodine, calcium, and soft tissue. On the other hand, ED represents the electron density of a tissue with respect to water and is expressed on a percentage basis (%EDW); water will have an ED value of 100.[19]

Zeff information has led to substantial improvement in imaging in different clinical areas. It has helped in the diagnosis of kidney stone composition. The separation between uric acid and calcium-based stones has been enhanced using Zeff information.[20,21] On the other hand, ED maps of tissues aid in the planning of radiotherapy yielding an accurate estimation of the tissue stopping power to charged particles.[12,15] Regarding BMD and osteoporosis studies, spectral-CT has been used to assess the accuracy of BMD estimations in phantom studies,[22,23] but to the best of our knowledge, no spectral-CT applications have been published on calcium-based implants.

We hypothesized that spectral-CT techniques can enhance the separation between resorbable calcium-based implants and bone compared with standard QCT. With this study we aimed to:

- Establish methods to characterize the separability of calcium-based implants and bone in a close-to-clinical setting to apply them in future studies using AGN1 as an example of a resorbable calcium-based implant material.
- Compare the separability power between AGN1 and bone (compact and cancellous) using spectral-CT techniques in the form of Zeff or ED maps in contrast to conventional uncalibrated (HU) and calibrated (BMD) reconstructions.

This study may aid in future in vivo monitoring of resorbable, osteoconductive implants, and resultant new bone formation.

Materials and Methods

Theoretical modeling of effective atomic number (Zeff)

Zeff estimations have been used to model surrogate materials and biological tissues. Theoretical models are often based on power-law formulas, where Zeff is dependent on the constituents of the mixture or composition.[18] However, it is known that such formulae oversimplify the photon/matter interactions, which are energy dependent.[24] In other words, the Zeff of a mixture or compound depends on the photon energy of the X-ray spectrum. Despite such limitations, we aimed at calculating a theoretical Zeff of our materials of interest, namely bone, bone marrow, and the calcium-based implant AGN1, by using two formulas. One formula followed Mayneord (as in formula 1 in Schaeffer and colleagues[18]) and a second formula was adapted from Landry and colleagues[15] (see Appendix S2). We calculated theoretical values for our materials and compared them to data reported in the literature, obtained either from experimental Zeff measurements or from known compositions; eg, as provided by the bone density calibration (BDC)-phantom manufacturer. The BDC is a QCT-calibration phantom composed of three rods with

different amounts of calcium hydroxyapatite and a solid-water surrogate; it was scanned in the two CT sessions of our study to calibrate BMD measurements. The main goal of deriving theoretical Zeff values was to verify our experimental measurements.

Specimen acquisition and CT protocol

Ten denuded cadaveric human femurs (six right [6R] and four-left [4L] anatomical sides) were used for the study. All of the femurs were from male donors who had been recruited by the body donation program at the Institute of Anatomy, Christian-Albrechts University of Kiel. Written consent for use for educational and research purposes had been obtained from the donors. Preoperative CT scans of the frozen specimens were conducted using an IQon spectral-CT scanner (Philips Medical, Best, Netherlands) located at the emergency department of the University Medical Center Schleswig-Holstein (UKSH) in Kiel, Germany.

CT protocols for preoperative and postoperative scans were identical unless noted otherwise. CT acquisition settings were 120 kVp and 75 mAs, except for one specimen scanned with 200 mAs. The collimation width for all specimens was 0.625 mm × 64 slices with a spiral pitch factor of 0.203 (CT dose index, CTDIvol = 6.4 mGy). The CT table height was 86 cm. For the reconstruction, a 0.9 mm slice thickness with 0.45 mm increment was selected. The field of view (FOV) included the whole femoral sample and a BDC-calibration phantom (QRM, Moehrendorf, Germany) used for QCT measurements. Pixel spacing ranged across the samples from 0.352 to 0.406 mm in the preinjection scans and from 0.293 to 0.375 mm in the postinjection scans. A high-resolution bone kernel (YD) without metal-artifact or dose-reduction algorithms was selected. Spectral-CT data of each CT scan were exported as spectral base image (SBI) files, a proprietary Philips data file, from which Zeff and ED reconstructions were generated. Conventional CT reconstructions in Hounsfield units were analyzed for comparisons with spectral-CT data and used as input to the QCT BMD measurements. The actual calibration of Zeff and ED was performed by the spectral-CT scanner manufacturer (Philips) using proprietary algorithms and additional calibration measurements.

Implant material injection and postinjection CT procedures

After the completion of the preoperative CT scans, the cadaveric femurs were transferred to the Department of Anatomy, CAU Kiel and stored frozen at −20°C. To partially approximate surgical conditions the frozen specimens were thawed at 4°C for 48 hours and then allowed to reach room temperature before the AGN1 injection. AGN1 injection was performed by a trained trauma surgeon in a setting approximating clinical surgery; C-arm fluoroscopic images were taken in the anteroposterior (AP) and lateral planes before, during, and at the end of the procedures. AGN1 was injected using methodology previously described in Stroncek and colleagues.[6] Briefly, under fluoroscopy, a 2.5-mm guide pin was inserted into the lateral aspect of the proximal femur, approximately 2 cm distal to the greater trochanter. The guide pin was advanced through the intertrochanteric region to the femoral neck. A 5.3-mm cannulated drill was advanced over the guide pin to create the access portal. A blunt probe debrider was used to loosen the bone marrow and nonstructural marrow elements, which were removed with sequential suction and irrigation. AGN1 was then manually injected into the enhancement site in a backfilling motion. Hence, similar to the clinical scenario, the injected AGN1 implant material occupied the missing marrow and cancellous bone space. Procedural details such as timing of each step and volume of AGN1 injected were collected. The AGN1 material was allowed up to 7 hours to harden before freezing the samples at −20°C. After the implant injection procedures had been completed the samples were transported while frozen to the CT scanner for the postoperative CT scans. The postoperative CT session was completed within 2 hours, after which the samples were taken back to the Anatomy institute for further freezing at −20°C.

Image analysis

Using the custom developed in-house software Structural*Insight* (used in many clinical studies over the past decades[25-28] and that can be made available to interested readers upon a reasonable request: https://www.moincc.de/equipment/imaging-software/structural-insight) the conventional CT reconstructions of both sessions were calibrated to HA equivalent BMD (mg HA/cm^3) by means of the BDC-calibration phantom scanned concurrently with the samples. Image segmentation and registration in this study were conducted with 3D Slicer[29] as detailed below in this section. In order to characterize the density range of the samples BMD was assessed within a femoral neck volume of interest (VOI) using similar locations to the ones used in dual-energy X-ray absorptiometry (DXA) or QCT scans. Apart from this VOI, we identified four other VOIs used for evaluations of both the preoperative and postoperative injection CT data. Image segmentation for these four VOIs was performed by one operator using the postoperative conventional CT volumes (as only in the postinjection CTs contours for the AGN1 implant material could be drawn) and included the following regions: (VOI 1) AGN1 injection site, (VOI 2) compact bone at the femoral shaft, (VOI 3) femoral head cancellous bone, and (VOI 4) bone marrow at the femoral shaft (Fig. 1). For the AGN1 implant material, VOI 1, the segmentation process included "level-tracing" to delineate contours of the implant material in two dimensions (2D) across several slices. This "level-tracing" tool identified a closed path around the implant that had uniform intensities tracing back to the selected starting pixel. This step was repeated across several nonadjacent slices to define a starting point of a region growing algorithm ("grow-from-seeds") for AGN1. In parallel, regions outside the implant material, within the cancellous region, were manually marked across several slices. Using the "grow-from-seeds" tool for the two regions marked, yielded the delineation of the AGN1 VOI. This process was iterative, improving the regions marked in 2D across several slices until an optimum three-dimensional (3D) segmentation of AGN1 was obtained. The volume of AGN1 (VOI 1) was determined and served as basis for the size of VOI 2–VOI 4, to approximately match the same volume. Thus, VOI 3 covered volumes at the femoral head using spheres, whose radii ranged from 8.7 to 14.9 mm. VOI 2 and VOI 4 extended distally at the femoral shaft starting from around 30 mm caudal to the lesser trochanter with lengths that ranged between 4.7 and 40.4 mm to between 10.9 and 69.3 mm, respectively, and which depended on the femur sample. VOI 2, compact, was obtained first by selecting a box-like VOI over the femoral shaft, then using a threshold of 800 HU to exclude the marrow region and finally by removal of trabecularized endosteal bone structures. Similarly, VOI 4, marrow, was obtained by selecting a box-like VOI over the femoral shaft and

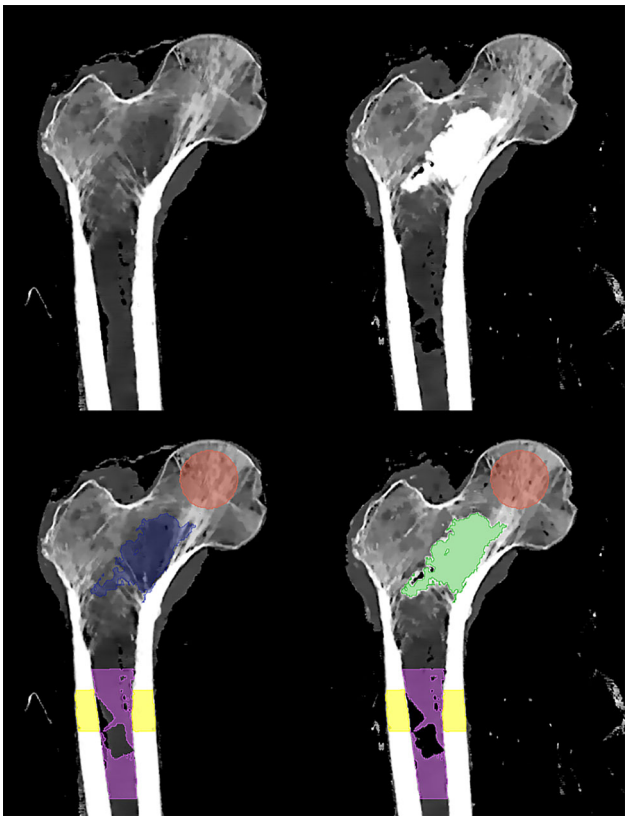

Fig. 1. Coronal views of Zeff maps from one femoral specimen for the (left) preoperative and (right) postoperative spectral-CT scans. (Bottom) Color-coded segmentations at the femoral head (red), femoral neck (injection site, pre: blue and post: green), bone-marrow (purple), and compact bone (yellow) at the femoral shaft.

using band-pass thresholding with low and high thresholds of −300 HU and 200 HU to exclude gas inclusions and compact bone, respectively. A final manual correction was also performed for this VOI. Subsequently, 3D image registration was conducted keeping the preoperative conventional CT as the fixed and transforming the postoperative CT volumes to match them to their preoperative counterparts. An affine-3D transformation was thus obtained and applied to the segmented VOI 1 through VOI 4 resulting in a mapping of these VOIs to the corresponding anatomical location of the preoperative CT volumes. In this way, for the preoperative CT scans, VOI 1 was located mainly at the femoral neck with only minor contributions from the intertrochanteric region. It is thus referred to as cancellous femoral neck (Cancellous FemNeck). Furthermore, VOI 2 as measured in the preoperative CT scans is hereafter referred to as Compact. For all segmented VOI 1–VOI 4 average HA-equivalent density (ie, BMD), HU, ED, and Zeff values were derived. Histograms were calculated for BMD, HU, ED, and Zeff techniques directly from the CT volumes and segmentation masks using custom written scripts in MATLAB (version 2019a; The MathWorks Inc., Natick, MA, USA).

Statistical analysis

The mean and standard deviation of the voxel intensities were calculated within every VOI of each sample and for each CT technique on the preoperative and postoperative CT scans. Statistical nonparametric tests were performed to test for the differences before and after injection at the injection site (Cancellous FemNeck VOI) for each technique. To assess overall differences but also include overlap patterns between two distributions, eg, AGN1 and bone, we used receiver-operating characteristic (ROC) curves. ROC was chosen as the analysis tool for separability because of two main reasons. First, simpler overlap metrics of histograms do not reflect the shape of histogram distributions. For example, for improved separability sharper peaks are preferable to broad distributions with long tails. Such tails may limit discrimination of, eg, bone from AGN1, while still providing significant differences in the histogram distributions, if the main peaks are sharp and well resolved from other peaks. For the ROC analysis, sensitivity and specificity were calculated across the entire range of voxel intensities from the lowest to the highest threshold; ie, from one tail end of the distribution all across to the other tail's end. Second, the area under the curve (AUC), a frequently used metric in ROC analyses, can be directly translated into a separability metric with values of 1.0 illustrating a perfect separation of AGN1 from bone and values close to 0.5 a poorer separation performance. We thus imported the calculated histograms into R[30] for the following VOIs: Cancellous FemNeck and Compact (both from the preoperative CT scans) and AGN1 (from the postoperative CT scan). We quantified the separability of AGN1 from cancellous (ie, pair of regions *AGN1 – Cancellous FemNeck*, measured at the AGN1 injection site) and compact (ie, pair of regions *AGN1 – Compact*) bone. Using vertical averaging[31] mean-ROC curves were calculated for the conventional and spectral techniques for the two pairs of regions discussed. The AUC separability metric of these pairs of regions was calculated for each of the conventional and spectral-CT techniques. Because of the low number of samples ($N = 10$) we did not assume the normality of the underlying distribution of the AUC values. Moreover, the AUC separability metric has some degree of skewness and is bounded to a maximum value of 1.0. Therefore, we used the more robust statistical non-parametric (signed paired Wilcoxon) test for differences between techniques in the AUC. For an $\alpha = 0.05$, the significance level was established at a p value $< \alpha/n$, where n is the total number of comparisons (Bonferroni adjustment for multiple comparisons). Hence, for a total number of six comparisons (for four techniques) p values < 0.0083 were deemed significant. We present in Appendix S1 of this work corresponding results for the comparisons between AGN1 and femoral head cancellous bone (*AGN1 – Cancellous FemHead*).

Statistical analyses were conducted in JMP Pro (v16.0; SAS Institute, Cary, NC, USA) except for the ROC analyses and tests which were performed in R using the pROC package.[30,32]

Results

Sample and VOI characteristics

The average age of the donors was 83.5 years with a broad range of BMI and femoral BMD values (see Table 1). The mean ± SD volume of AGN1 injected into the proximal femurs was 14.3 ± 6.4 cm^3 and ranged from 4.0 to 20.0 cm^3. Figure 1 illustrates coronal Zeff maps obtained from the spectral-CT reconstruction of a representative femoral specimen before and after application of the AGN1 implant. Color overlays represent the segmented VOI 1–VOI 4 (see section Image analysis) at the cancellous AGN1 implant injection site (mostly at the femoral

Table 1. Sample Characteristics of Donors and Bone Mineral Density Estimated From QCT Volumes of Interest at the FN ($N = 10$)

Parameter	Age (years)	Weight (kg)	Height (cm)	BMI (kg/m^2)	BMD_FN (mg HA/cm^3)
Mean	83.90	63.20	169.40	21.95	125.32
SD	8.97	20.50	7.01	6.32	57.18
Range	[75, 100]	[45, 113]	[160, 177]	[14.7, 36.1]	[55.66, 241.71]

FN = femoral neck.

neck), compact bone, cancellous femoral head, and bone marrow in the shaft. Note that the use of image registration allowed for an accurate analysis by placing VOIs at exactly the same spatial locations on the femurs in the two CT scans, thus minimizing variability in the measurements.

Accuracy and precision of Zeff and EDW

In Table 2, we report the expected values of Zeff based on their chemical composition using two different approaches by Mayneord and Landry and colleagues.[15] For comparison, Table 3 shows descriptive statistics for the experimental data on Zeff, along with results for BMD, HU, and ED in the four VOIs. The average Zeff measured in the compact bone region was around 13.1 Zeff units, comparable to values reported for cortical bone in the literature and within the expected variability of 0.2 Zeff units reported by the CT manufacturer for spectral-CT analysis data.[19] Average bone-marrow was −9.5 HU in the preoperative CT scan. This negative mean HU value indicates the presence of yellow (fatty) bone-marrow in the samples as expected from the age of the specimen donors. Consequently, the mean BMD of marrow was also negative. The fatty bone-marrow showed a lower EDW than water (100) and a Zeff between that of pure fat and water; ie, 5.9 and 7.4 Zeff units,[19] respectively. For an assessment of precision, we analyzed two repeated measurements in regions not affected by the implant treatment (marrow, compact, and femoral head): their average values before and after implant injection differed at most by 9 HU or 6 mg HA/cm^3, 0.5 EDW, and 0.02 Zeff units, respectively. In Appendix S2, Table S1 shows summary results of the average absolute and relative differences for each region and CT technique.

Discrimination of bone from AGN1 implant material

Figure 2 shows histograms calculated from the VOIs depicted in Fig. 1 for conventional, calibrated (BMD) and uncalibrated (HU) and for spectral (ED and Zeff) reconstructions of a representative femoral specimen. Histograms depict the voxel intensities in those regions before and after the AGN1 injection. Consequently, only the histograms at the injection site (labeled Canc. FemNeck in the preinjection [blue] and AGN1 in the postinjection [green] graphs) changed appreciably. The peaks of the spectral-CT techniques ED and Zeff (marrow [purple] and AGN1 [green]) were substantially sharper compared to the corresponding peaks of BMD and uncalibrated CT numbers and thus resulted in less overlap. Most importantly, the distinction between AGN1 and compact (cortical) bone can be clearly appreciated from the histogram of Zeff (Fig. 2 bottom right). The main peak position for most samples was around 14.0 or higher for AGN1 and 13.3 Zeff units for compact bone. For cancellous bone of the femoral head and femoral neck not one marked single peak but rather multi-peaks were observed (Fig. 2 blue and red distributions) that ranged from 8.0 to 11.4 and from 7.0 to 9.3 Zeff units, respectively. The main peak for bone marrow was around 6.7 Zeff units.

At the AGN1 injection site, substantial increases in BMD and uncalibrated CT numbers were observed between preinjection and postinjection scans with average changes of 1164 mg

Table 2. Theoretical and Calculated Zeff Values For the Triphasic Calcium-Based Implant AGN1, Its Main Components (Calcium Sulfate, TCP: β-Tricalcium Phosphate and Brushite), and the Principal Bone Mineral Component Calcium HA

Parameter	Molecular formula	Zeff literature	Zeff calc Mayneord[a]	Zeff calc Landry[b]
AGN1		NA	15.11	15.08
Calcium sulfate	$CaSO_4$	NA	15.22	15.22
TCP	$Ca_3(PO_4)_2$	NA	15.81	15.81
Brushite	$(CaHPO_4)\cdot 2H_2O$	13.82[c]	13.97	13.82
Bone (Cortical, ICRU-46)		13.2[d]	13.39	13.23
Bone-mineral (HA)	$Ca_{10}(PO_4)_6(OH)_2$	15.86[c]	15.87	15.86
Water (liquid)	H_2O	7.4[d]	7.68	7.42
Solid water		7.4[d]	7.60	7.40
BDC Phantom				
SWE	NA	6.95[e]	7.16	6.95
SWE + 100 mg HA	NA	8.56[e]	8.80	8.56
SWE + 200 mg HA	NA	9.66[e]	9.91	9.66

NA = not available; SWE = Solid-water equivalent.
[a]Mayneord's formula with m = 2.94.
[b]Johns and Cunningham (1983) and Landry (2013) with β = 2.94.[15] Solid water composition using values from Table 1 in Landry and colleagues.[15]
[c]Using weighted average of atomic numbers, values taken from Qu and colleagues.[21]
[d]Values taken from Vlassenbroek.[19]
[e]Values and compositions provided by the BDC phantom manufacturer (QRM).

Table 3. Mean ± SD Calculated Over the Segmented Regions For Conventional and Spectral-CT Techniques ($N = 10$)

Parameter	Conventional BMD (mg HA/cm^3)	Conventional uncalibrated (HU)	Spectral ED (%EDW)	Spectral Zeff (Zeff units)
Preoperative				
Total proximal femur	180.51 ± 68.38	268.71 ± 95.44	110.69 ± 5.08	8.73 ± 0.42
Cancellous femoral neck[a]	69.54 ± 35.63	109.16 ± 49.78	104.38 ± 2.52	8.30 ± 0.41
Compact	1124.15 ± 71.42	1648.63 ± 97.76	177.13 ± 5.18	13.06 ± 0.16
Cancellous femoral head	243.07 ± 105.6	357.46 ± 147.47	116.43 ± 7.1	9.80 ± 0.79
Marrow	−9.49 ± 7.24	−4.60 ± 9.69	97.06 ± 1.18	6.87 ± 0.28
Postoperative				
Total proximal femur	241.10 ± 54.59	356.97 ± 76.65	115.76 ± 3.81	9.12 ± 0.35
AGN1 femoral neck[a]	1233.12 ± 66.69	1741.12 ± 103.31	181.27 ± 5.23	13.55 ± 0.14
Compact	1129.39 ± 69.91	1657.82 ± 97.58	177.68 ± 5.38	13.08 ± 0.16
Cancellous femoral head	236.94 ± 105.66	352.91 ± 148.91	116.12 ± 7.3	9.81 ± 0.78
Marrow	−11.36 ± 4.25	−4.08 ± 6.11	97.55 ± 0.55	6.84 ± 0.29

The "total proximal femur" region comprised bone-marrow, soft-tissue remnants, and cancellous and cortical bone.
[a]Injection site, mostly at the femoral neck and the intertrochanter region.

HA/cm^3 for BMD (>2000%, $p < 0.002$) and 1632 HU for uncalibrated CT numbers (>1800%, $p < 0.002$). Corresponding increases for the spectral measurements were 77 EDW (+74%, $p < 0.002$) and 5.25 Zeff units (+64%, $p < 0.002$). The differences between AGN1 and compact bone were 109 mg HA/cm^3 (+10.1%, $p = 0.01$) for BMD and 92 HU (+6%, $p = 0.105$) for uncalibrated CT numbers; for spectral measures differences were 4.1 (+2.4%, $p = 0.105$) for ED and 0.49 (+3.7%, $p = 0.002$) for Zeff.

Improved performance in the separation of bone from AGN1 using spectral-CT was reflected in the results of the ROC analysis presented in Fig. 3*A*,*C*, showing four ROC curves (each averaged across 10 samples) for BMD, HU, Zeff, and ED techniques. Figure 3*A*,*B* depicts the discrimination of AGN1 versus cancellous bone (regions AGN1 – Cancellous FemNeck) and Fig. 3*C*,*D* of AGN1 versus cortical (compact) bone (regions AGN1 – Compact). The area under the curve (AUC) of Zeff was significantly larger than that of BMD, HU or ED, both for cancellous and compact bone. The improvements in the AUC separability metric using Zeff are also apparent in Fig. 3, right side, where the distribution of AUCs obtained from the corresponding ROC curves is plotted for each of the 10 femoral samples. Because of the substantial increase in the measured values for all techniques when changing from cancellous bone to AGN1, i.e., pair of regions AGN1 – Cancellous FemNeck, all resulting AUCs for this comparison allowed a near-to-perfect discrimination; ie, very close to 1. Still, using either DeLong's or the bootstrap test for comparing ROC curves between Zeff and either BMD, HU, or ED highly significant p values ($p < 0.0001$) were observed. The AUC levels for each sample for Zeff in the cancellous regions were larger than for any other technique (Fig. 3*B*) and the advantage was even more pronounced when looking at the compact bone region (Fig. 3*D*).

Table 4 shows summary numerical results of the AUC metric. The results of the Wilcoxon paired signed rank statistical tests performed can be summarized as follows. AUC of Zeff was significantly larger than the AUC of either BMD, HU, or ED for both pairs of regions analyzed (all p values < 0.002). The statistical tests for AUC differences of BMD versus HU or versus ED were significant for the region Compact (both $p < 0.002$) but not for Canc. FemNeck: BMD versus ED ($p = 0.014$), BMD versus HU ($p = 0.064$). The AUC between ED and HU was not significantly different for the Canc. FemNeck ($p = 0.027$) nor for the Compact ($p = 0.084$) region.

In the Appendix S1 of this work, we present the separability metric AUC between AGN1 and femoral head cancellous bone (AGN1 – Canc. FemHead) and note here that it followed a similar pattern as for Canc. FemNeck. Mean ± SD AUC for Zeff was 0.9896 ± 0.0116 compared to 0.9819 ± 0.0189, 0.9812 ± 0.0195, and 0.9770 ± 0.0249 for BMD, HU, and ED, respectively. This AUC observed for Zeff was significantly larger compared to BMD, HU, or ED, (Fig. S1 and Table S1 in Appendix S1).

Discussion

We have developed and tested an imaging analysis approach for effective atomic number, Zeff, and electron density data obtained from a dual-layer spectral CT device. The aim was to improve the separability between AGN1, a resorbable calcium-based implant, and bone. Our study was conducted using an ex vivo setting to approximate surgical procedures currently performed in patients in vivo. We documented that Zeff maps can effectively separate AGN1 from cancellous and even compact bone by showing positive prediction values and AUCs > 0.5 for all samples in this study. We also demonstrated significantly superior performance of Zeff compared to conventional CT measures, including calibrated BMD and uncalibrated CT data. Therefore, we would argue that spectral-CT represents a substantial advance in quantitative imaging in the field of bone implant imaging and potentially even beyond.

One goal of our study was to address the need of diagnostic methods to monitor resorbable and osteoconductive implants over time and in vivo. We focused on resorbable materials because on the one hand the assessment of metal-based implants is compromised when using X-ray-based techniques because of their strong X-ray absorption. On the other hand, as noted by Varga and colleagues,[2] nonmetallic implants may be a better option for augmentation at the proximal femur, for example femoroplasty with calcium-based implants or other materials, because the mechanical properties of such materials are closer to bone.

In vivo assessments of calcium-based implant material resorption would benefit from techniques that can differentiate the implant material from native bone. Separation, or in other words segmentation of implant material from bone using standard QCT

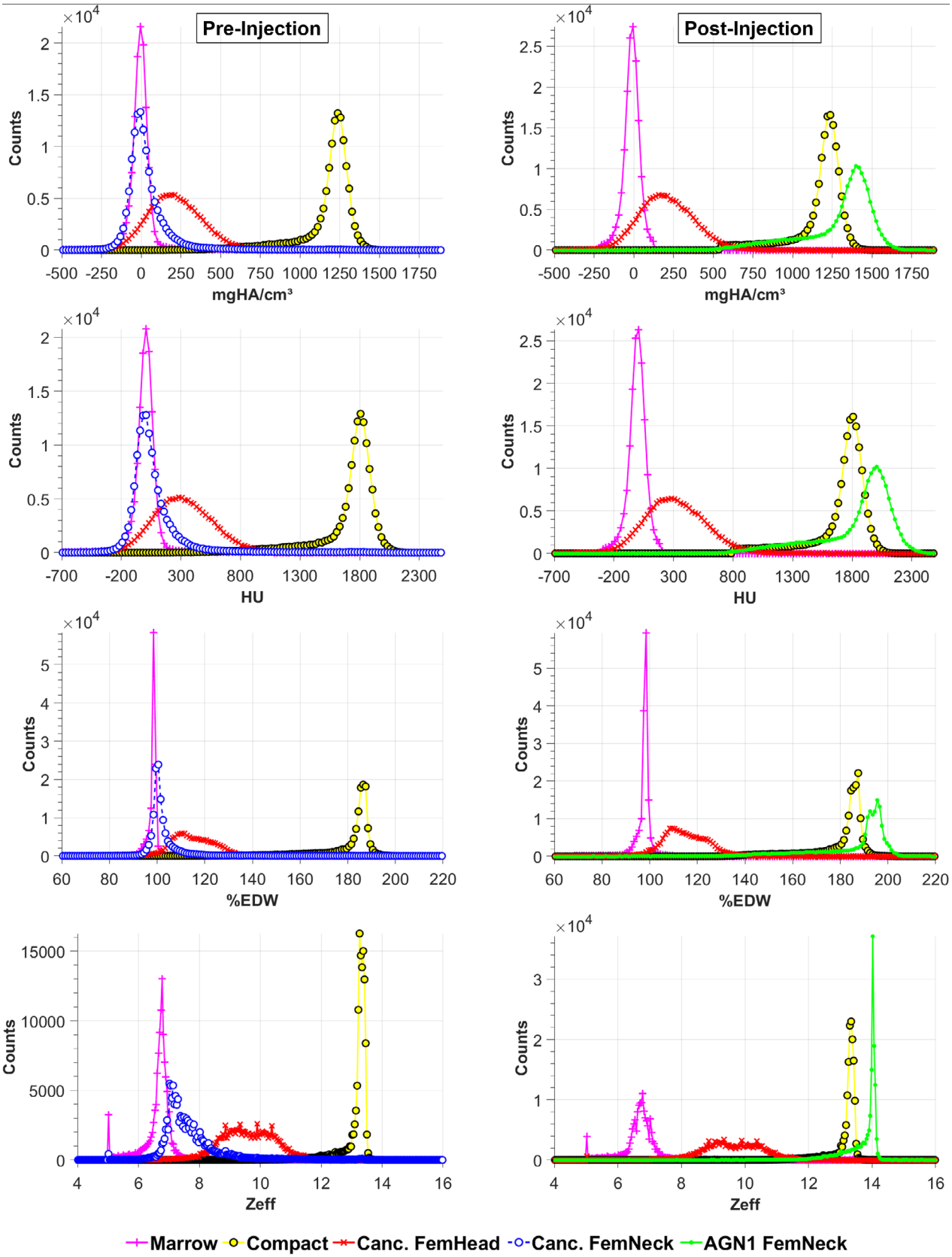

Fig. 2. Histograms obtained from the regions segmented and depicted in Fig. 1 for one representative femoral sample. (Left) Preoperative and (right) postoperative CT volumes. From top to bottom: Conventional calibrated (mg HA/cm^3) and uncalibrated (HU); spectral electron density (EDW); and effective atomic number (Zeff).

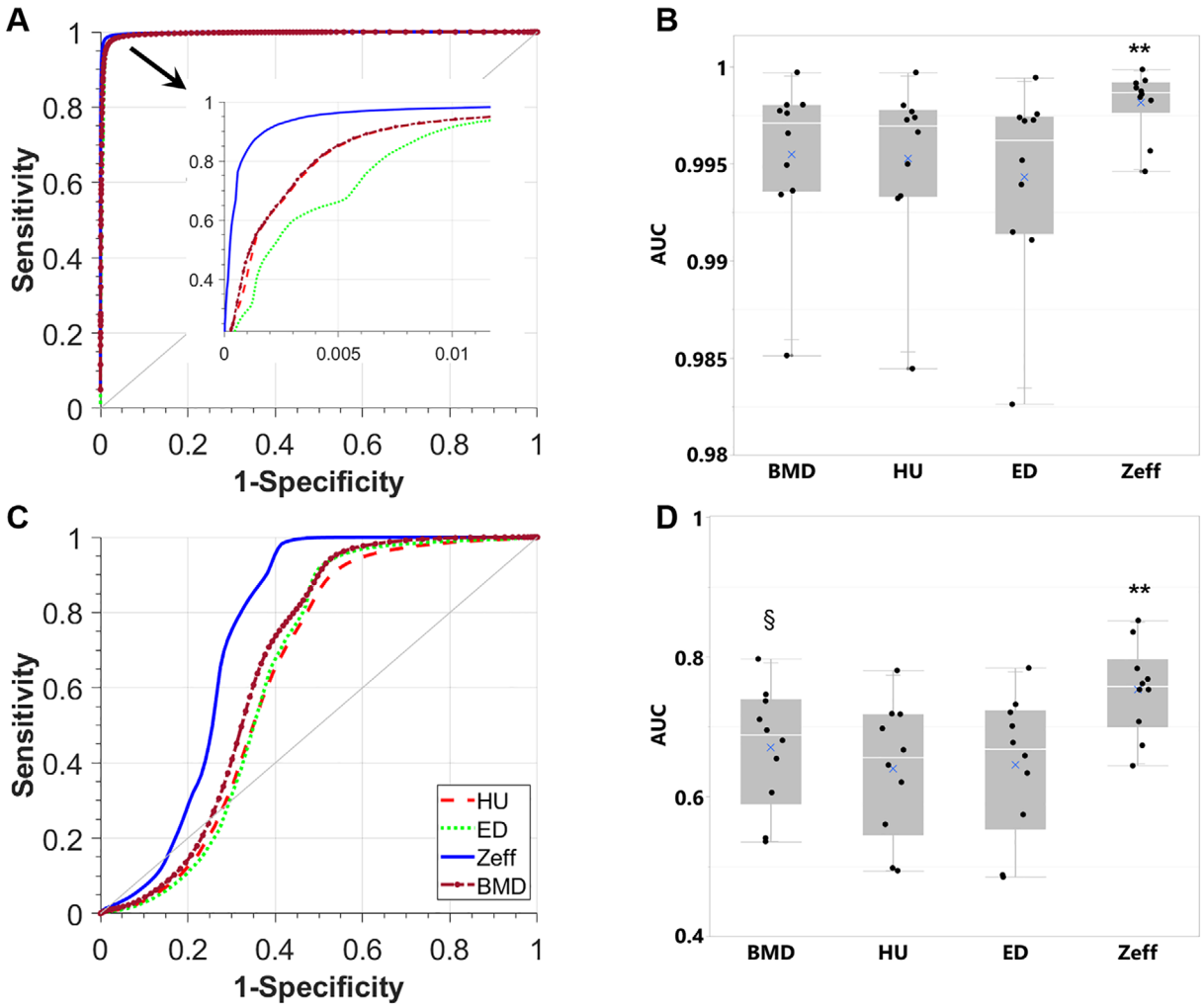

Fig. 3. (*A*,*C*) Mean-ROC curves and (*B*,*D*) AUC separability metric that illustrate the discrimination between AGN1 and cancellous FemNeck (at the injection site) (*A*,*B*) and between AGN1 and compact bone (at the femoral shaft) (*C*,*D*) when using spectral (Zeff, ED) and conventional (BMD, HU) CT volumes. **Statistically significant greater AUC values were observed when comparing Zeff with either BMD, HU, or ED (all $p < 0.002$). §Statistically significant greater AUC values when comparing BMD with HU or ED (all $p < 0.002$). Significance level was regarded in these comparisons after Bonferroni correction for multiple comparisons, see section Statistical analysis. FemNeck = femoral neck.

Table 4. Mean ± SD of the Separability Metric AUC From ROC Curves Obtained From the Distributions of Femoral Neck Cancellous Bone and AGN1 (AGN1 – cancellous femoral neck) and Compact Bone and AGN1 (AGN1 – Compact) with BMD, Uncalibrated CT Numbers (HU), and Spectral (ED and Zeff) CT Techniques ($N = 10$)

Pair of regions	AUC BMD	AUC HU	AUC ED	AUC Zeff
AGN1 – Cancellous femoral neck	0.9955 ± 0.0042	0.9953 ± 0.0043	0.9943 ± 0.0049	0.9981 ± 0.0017
AGN1 – Compact	0.6700 ± 0.0869	0.6397 ± 0.0967	0.6452 ± 0.1013	0.7529 ± 0.0651

is challenging because of their similar radiopacity. On the other hand, this separation of bone from implant could be important to monitor the changes at the implant site over time. New bone formation as the implant resorbs was demonstrated for AGN1 using histology in preclinical studies, correlating with changes in biomechanical properties.[9] Although clinical testing has shown apparent resorption and bone formation paired with increases in BMD after injection in postmenopausal osteoporotic women,[1] confirmatory clinical histology and biomechanical testing has not been possible to date. Therefore, development of new and clinically applicable techniques to distinguish calcium-based implant materials from native bone would improve the evaluation of the effectiveness of such materials to replace osteoporotic bone loss. One step toward these goals is the analytical separation between bone and implant as documented in this study.

As such, resorbable implants are targeted at osteoporotic bone with low density and deteriorated bone structure. The comparisons of AGN1 versus cancellous bone in the femoral neck region, ie, the bone replaced by the injected material, demonstrated a high separability for all techniques (mean AUC > 0.99, Table 4). This means that separability between newly injected implant and cancellous bone is already possible using conventional CT. However, one must consider that the cancellous bone at the treatment site of the samples, and most probably also in osteoporotic patients, is mainly composed of bone-marrow, cf. marrow and Canc. FemNeck curves in the histograms of Fig. 2. A denser cancellous structure was assessed in the femoral head region. As can be observed for BMD (Fig. 2, top row), its distribution (in red) partially overlaps with that of cancellous bone of the femoral neck (in blue) and even partly with the low-end tail of the AGN1 distribution (in green). Zeff features much sharper distributions and less overlap (Fig. 2, bottom row). What could happen when there is new bone formed at the implant site? To address this question, we performed the most extreme comparison; ie, testing whether AGN1 could even be distinguished from almost pure compact bone. It is almost pure bone tissue because very small pores are disregarded as they cannot be resolved by our CT imaging resolution in the femoral shaft and at the AGN1 injection site. Nonetheless, the separability estimations here represented a worst-case scenario of two very similar radiopaque and dense materials. Our AUC metric analysis showed that they were significantly better separated using Zeff (mean AUC = 0.75) compared to conventional CT techniques (mean AUC ranging from 0.64 to 0.67), see Table 4. Hence, in future studies in patients, newly formed bone should be better separated from the implant using spectral Zeff maps compared to conventional CT approaches. Of course, even with Zeff one will have to deal with partial volume effects like in conventional CT. However, with the new Zeff approach one should be able to better investigate one key question regarding the use of such implants: whether new bone is formed at the border of the injection site. Given the expected layer-by-layer degradation of the implant material from the outside to the inside and the resulting decrease in BMD and Zeff, any observed increase near the vicinity of the remaining implant could be interpreted as newly formed bone. As for the possible infiltration or insertion of implant between trabecular bone during surgery, this may not be a problem if such trabecular bone would contribute equally to the Zeff distributions at baseline and follow-up. Furthermore, increases in the histogram in the range of Zeff values typical for bone observed near the AGN1 region could be considered indicative of osteogenic processes. For information on bone formation in patients, non-invasive imaging methods are continuing to be developed; this is exactly where the spectral-CT information will be most relevant. Because of the differences in methodology, there are no systematic assessments of longitudinal changes available yet for patients.

With respect to the bone/implant separability the ED maps did not perform as strongly as their Zeff counterparts. Zeff captures the chemical differences in the material, whereas ED demonstrates density differences, which may be equivalent to that provided by BMD or HU. Other applications may as well involve ED values of the implant materials and the values calculated here for human femurs and AGN1 may serve as reference for other studies or similar applications. We did not evaluate other types of spectral-CT data, for example virtual monoenergetic images.

Average values of BMD, uncalibrated CT numbers, ED, and Zeff at nontreated sites of the femurs were similar before and after surgical procedure. Using image registration as an enabling analysis tool for longitudinal treatment studies is worthwhile. As was the case for our study, whenever consistent accurate measurements (in our case of Zeff, ED, BMD, or HU) are needed, image registration can help in revealing small changes in longitudinal studies that could otherwise remain unnoticed. Therefore, in future in vivo studies a possible analysis pipeline could encompass the following steps: template segmentation or VOI definition at a baseline CT measurement; use of image registration to assess that same VOI in follow-up scans and use of spectral-CT that provide Zeff maps. This analysis pipeline may aid at quantifying implant resorption and new cancellous bone formation.

Our study had some limitations. Segmentation errors can influence the outcomes of our ROC assessments. Region inhomogeneities in the implant mixture as well as compressed trabecular bone debris formed during reaming and debridement in the surgical procedure can lead to errors in the segmentation of the implant material. In the histograms of some samples a long AGN1 "shoulder" was observed that flared out at densities and Zeff values smaller than the main peak position. Additional or more refined segmentation steps may reduce this effect. However, for our analysis this source of error would affect all techniques similarly. A key remaining question is, whether our observations would still remain valid and translatable to in vivo applications. We conducted the experiments as similar as possible to the clinical setting and it will be possible to use the same type of CT scanner and protocol in patient studies. Despite all donors from this study being males, the wide range of BMD values observed at the total proximal femur (57.85 to 207.23 mg HA/cm^3, Table 1), highlight the possibility to translate these results to patients with very different levels of bone status. The physiological temperature of 37°C could not be accomplished for with our samples during the experiments (injected at room temperature and CT scanned while frozen). Different temperatures might play a role for Zeff properties, especially of soft tissue and bone-marrow. For cortical bone, our Zeff measurements were very close to the values reported in the literature (Table 2) and our measurements showed agreement with the theoretical model used. The cadaveric specimens were denuded and a surrogate tissue or a water tank was not employed to represent soft-tissue during the CT scans. Finally, the methods described herein were restricted to only AGN1, a calcium-based implant material. This study did not examine other resorbable, osteoconductive materials for example magnesium-based. In the future, further spectral-CT applications like the one presented here may have to cross-calibrate measurements of Zeff or ED when pooling data from different CT manufacturers.

In summary, our study suggests that spectral-CT, in particular Zeff, provides substantially improved image analysis options for the assessment of calcium-based and perhaps other resorbable implant materials for in vivo longitudinal studies. Compared to BMD, Zeff enhances the separability of the calcium-based implant material tested and bone, both cancellous and cortical. These results warrant consideration of spectral-CT in patients undergoing treatment with similar calcium-based, resorbable, osteoconductive implant materials.

Acknowledgments

We acknowledge the help and support of the following persons for the conduction of this study: Stefanie Gundlach, Merle

Winkler (Anatomy Institute CAU, Kiel) for assistance with the sample preparations and injection procedures; Tristan Klintz, Florian Becker, Gesa Peleikis and Sabrina Vogelsang for assistance during the CT scans; Prof. Frank-André Siebert (UKSH, Kiel) for advice on theoretical calculations on spectral-CT data and Falk Dukatz (AgNovos Healthcare) for assistance during the injection procedures. Open Access funding enabled and organized by Projekt DEAL.

Author Contributions

Jaime A Peña: Conceptualization; data curation; formal analysis; investigation; methodology; project administration; software; validation; visualization; writing – original draft; writing – review and editing. **Jonathan L Shaul:** Conceptualization; project administration; resources; supervision; writing – original draft; writing – review and editing. **Michael Müller:** Investigation; methodology; resources; writing – review and editing. **Timo Damm:** Formal analysis; methodology; software; writing – review and editing. **Reinhard Barkmann:** Formal analysis; methodology; writing – review and editing. **Bodo Kurz:** Investigation; methodology; resources; writing – review and editing. **Graeme M Campbell:** Methodology; resources; software; writing – review and editing. **Sandra Freitag-Wolf:** Formal analysis; methodology; software; writing – review and editing. **Claus-C Glüer:** Conceptualization; formal analysis; funding acquisition; methodology; project administration; supervision; writing – original draft; writing – review and editing.

Conflicts of Interest

JLS is an employee and shareholder of AgNovos Healthcare. GMC is an employee of Philips GmbH Market DACH.

Peer Review

The peer review history for this article is available at https://publons.com/publon/10.1002/jbmr.4710.

Data Availability Statement

Processed data that support the findings of this study are available on request from the corresponding author. The data are not publicly available due to privacy or ethical restrictions. Raw (unprocessed) data are not shared.

References

1. Howe JG, Hill RS, Stroncek JD, et al. Treatment of bone loss in proximal femurs of postmenopausal osteoporotic women with AGN1 local osteo-enhancement procedure (LOEP) increases hip bone mineral density and hip strength: a long-term prospective cohort study. Osteoporos Int. 2020;31(5):921-929.
2. Varga P, Hofmann-Fliri L, Blauth M, Windolf M. Prophylactic augmentation of the osteoporotic proximal femur—mission impossible? Bonekey Rep. 2016;5:854.
3. Sohn H-S, Oh J-K. Review of bone graft and bone substitutes with an emphasis on fracture surgeries. Biomater Res. 2019;23(1):9.
4. Fomin AS, Fadeeva IV, Filippov YY, et al. Brushite cement based on β-TCP for orthopedics. Inorganic Materials Applied Research. 2017;8(2):292-295.
5. Bohner M. Resorbable biomaterials as bone graft substitutes. Materials Today. 2010;13(1-2):24-30.
6. Stroncek JD, Shaul JL, Favell D, et al. In vitro injection of osteoporotic cadaveric femurs with a triphasic calcium-based implant confers immediate biomechanical integrity. J Orthop Res. 2019;37(4):908-915.
7. Trost M, Schmoelz W, Wimmer D, Hörmann R, Frey S, Schulte TL. Local osteo-enhancement of osteoporotic vertebra with a triphasic bone implant material increases strength—a biomechanical study. Arch Orthop Trauma Surg. 2020;140(10):1395-1401.
8. Shaul J, Hill R, Bruder S, Tilton A, Howe J. Triphasic calcium-based implant material resorbs and is replaced with bone in ovariectomized rats with or without bisphosphonate treatment. J Orthop Res. 2022;40(10):2271-2280.
9. Shaul JL, Hill RS, Bouxsein ML, Burr DB, Tilton AK, Howe JG. AGN1 implant material to treat bone loss: resorbable implant forms normal bone with and without alendronate in a canine critical size humeral defect model. Bone. 2022;154:116246.
10. Mastrogiacomo S, Dou W, Jansen JA, Walboomers XF. Magnetic resonance imaging of hard tissues and hard tissue engineered bio-substitutes. Mol Imaging Biol. 2019;21(6):1003-1019.
11. Ma Y-J, Jerban S, Jang H, Chang D, Chang EY, Du J. Quantitative ultrashort Echo time (UTE) magnetic resonance imaging of bone: an update. Front Endocrinol. 2020;18(11):567417.
12. So A, Nicolaou S. Spectral computed tomography: fundamental principles and recent developments. Korean J Radiol. 2021;22(1):86.
13. Heismann BJ, Leppert J, Stierstorfer K. Density and atomic number measurements with spectral X-ray attenuation method. J Appl Phys. 2003;94(3):2073-2079.
14. Bazalova M, Carrier J-F, Beaulieu L, Verhaegen F. Dual-energy CT-based material extraction for tissue segmentation in Monte Carlo dose calculations. Phys Med Biol. 2008;53(9):2439-2456.
15. Landry G, Seco J, Gaudreault M, Verhaegen F. Deriving effective atomic numbers from DECT based on a parameterization of the ratio of high and low linear attenuation coefficients. Phys Med Biol. 2013;58(19):6851-6866.
16. Goodsitt MM, Christodoulou EG, Larson SC. Accuracies of the synthesized monochromatic CT numbers and effective atomic numbers obtained with a rapid kVp switching dual energy CT scanner: accuracies of DECT monochromatic CT numbers and Zeff. Med Phys. 2011;38(4):2222-2232.
17. Mei K, Ehn S, Oechsner M, et al. Dual-layer spectral computed tomography: measuring relative electron density. Eur Radiol Exp. 2018;2(1):20.
18. Schaeffer CJ, Leon SM, Olguin CA, Arreola MM. Accuracy and reproducibility of effective atomic number and electron density measurements from sequential dual energy CT. Med Phys. 2021;48(7):3525-3539.
19. Vlassenbroek A. Technical Aspects of Spectral CT. Spectral CT Clinical Case Collection [Internet]. [cited 2022 Mar 15]. p. 6-21. Available from: https://issuu.com/emmanuelcoche/docs/7709_phil19_coche_book_8-5x11_single_1003.
20. Joshi M, Langan DA, Sahani DS, et al. Effective atomic number accuracy for kidney stone characterization using spectral CT. Proceedings of the SPIE, Volume 7622, id. 76223K (2010). San Diego, California, United States. https://doi.org/10.1117/12.844372.
21. Qu M, Ramirez-Giraldo JC, Leng S, et al. Dual-energy dual-source CT with additional spectral filtration can improve the differentiation of non-uric acid renal stones: an ex vivo phantom study. AJR Am J Roentgenol. 2011;196(6):1279-1287.
22. Mei K, Schwaiger BJ, Kopp FK, et al. Bone mineral density measurements in vertebral specimens and phantoms using dual-layer spectral computed tomography. Sci Rep. 2017;7(1):17519.
23. van Hamersvelt RW, Schilham AMR, Engelke K, et al. Accuracy of bone mineral density quantification using dual-layer spectral detector CT: a phantom study. Eur Radiol. 2017;27(10):4351-4359.
24. Taylor ML, Smith RL, Dossing F, Franich RD. Robust calculation of effective atomic numbers: the auto- Z_{eff} software: auto- Z_{eff}: robust calculation of effective atomic numbers. Med Phys. 2012;39(4):1769-1778.
25. Graeff C, Timm W, Nickelsen TN, et al. Monitoring Teriparatide-associated changes in vertebral microstructure by high-resolution

CT in vivo: results from the EUROFORS study. J Bone Miner Res. 2007; 22(9):1426-1433.

26. Graeff C, Marin F, Petto H, et al. High resolution quantitative computed tomography-based assessment of trabecular microstructure and strength estimates by finite-element analysis of the spine, but not DXA, reflects vertebral fracture status in men with glucocorticoid-induced osteoporosis. Bone. 2013;52(2):568-577.
27. Glüer C, Marin F, Ringe JD, et al. Comparative effects of teriparatide and risedronate in glucocorticoid-induced osteoporosis in men: 18-month results of the EuroGIOPs trial. J Bone Miner Res. 2013; 28(6):1355-1368.
28. Krebs A, Graeff C, Frieling I, et al. High resolution computed tomography of the vertebrae yields accurate information on trabecular distances if processed by 3D fuzzy segmentation approaches. Bone. 2009;44(1):145-152.
29. Fedorov A, Beichel R, Kalpathy-Cramer J, et al. 3D slicer as an image computing platform for the quantitative imaging network. Magn Reson Imaging. 2012;30(9):1323-1341.
30. R Core Team. R: a language and environment for statistical computing [Internet]. Vienna, Austria: R Foundation for Statistical Computing Security; 2020. Available from:. https://www.R-project.org/.
31. Fawcett T. An introduction to ROC analysis. Pattern Recognit Lett. 2006;27(8):861-874.
32. Robin X, Turck N, Hainard A, et al. pROC: an open-source package for R and S+ to analyze and compare ROC curves. BMC Bioinformatics. 2011;12(1):77.